Electrochimica Acta 459 (2023) 142540

Contents lists available at ScienceDirect

Electrochimica Acta

journal homepage: www.journals.elsevier.com/electrochimica-acta

A facile preparation method and proof of cycle-stability of carbon-coated metal oxide and disulfide battery materials

Peng Guo [a,b], Lennart Singer [a], Zhiyong Zhao [c], Wojciech Kukułka [d], Finn Sebastian [a], Ewa Mijowska [d], Michael Zharnikov [c], Peter Comba [b,*], Rüdiger Klingeler [a,*]

[a] Kirchhoff Institute for Physics, Heidelberg University, Im Neuenheimer Feld 227, D-69120 Heidelberg, Germany
[b] Anorganisch Chemisches Institut, Universität Heidelberg, Im Neuenheimer Feld 270, D-69120 Heidelberg, Germany
[c] Angewandte Physikalische Chemie, Universität Heidelberg, Im Neuenheimer Feld 253, D-69120 Heidelberg Germany
[d] Nanomaterials Physicochemistry Department, West Pomeranian University of Technology, Piastów Av. 45, Szczecin 70-311, Poland

ARTICLE INFO

Keywords:
Lithium ion batteries
Tungsten-based materials
A facile method
Metal oxides
Metal disulfides

ABSTRACT

Constructing composites of metal oxides and disulfides with carbonaceous materials is considered a useful approach to improve their lithium-ion storage performance. However, complicated synthesis processes and high-cost carbonaceous materials usually used hinder the commercialization of such composites. Here, as an example, carbon-coated tungsten oxides and disulfides are prepared using a facile and simple method on the basis of two kinds of low-cost carbon sources (CTAB and PVP). Following our postulated synthesis route, a variety of carbon-coated WO_x, WS_2, as well as mixed-phase WO_x-WS_2 is presented. The CTAB-assisted WO_x/C (c-WO_x/C), WS_2/C (c-WS_2/C), and mixed-phase (c-WO_x/C-WS_2/C) electrodes exhibit outstanding capacity retention of 74%, 99%, and 95%, respectively, which still have 420 mAh g^{-1}, 460 mAh g^{-1}, and 525 mAh g^{-1} capacity left after 200 cycles at 100 mA g^{-1}. Particularly, the c-WS_2/C electrode exhibits superior long-term cycle stability of 97% retention after 500 cycles. Similarly, the PVP-assisted WS_2/C (p-WS_2/C) electrode displays a capacity retention of 80% after 500 cycles. This work provides an easy and versatile route to fabricate carbon-coated tungsten oxides and disulfides with compelling battery performance and can be easily implemented for other metal oxides and disulfides.

1. Introduction

The energy crisis arising from the depletion of fossil fuels, and environmental pollution force people to develop clean, renewable energy like solar and wind energy. To effectively use these energies, significant worldwide interest has been raised to have access to appropriate energy conversion and energy storage devices [1–4]. In particular, rechargeable lithium-ion batteries (LIBs) are promising energy storage systems for electric vehicles and electric grids due to their high energy density and super-long cycle life [5–7]. However, limited by the low theoretical capacity of graphite (372 mA h g^{-1}), which cannot meet the ever-growing demand for anode materials of next-generation LIBs, many endeavors have been placed on exploring alternative anode materials for LIBs [8–12]. Among them, metal oxides and sulfides, like tungsten oxide and tungsten disulfide, are promising candidates because of their high theoretical capacity (WO_3 - 693 mAh g^{-1}, WS_2 - 432 mAh g^{-1}), high intrinsic density, low cost, and environment friendliness [13–16].

However, fast capacity fading and poor rate performance caused by low electrical conductivity and large volume expansion during cycling hinder practical applications of these compounds. To solve these issues, constructing composite with carbonaceous materials has proven to be a promising strategy [17–19]. In previous work, most papers reported composites of metal oxides and sulfides with carbonaceous materials including graphene, carbon nanotubes (CNTs), and carbon fiber which worked as a substrate via in-situ growth or liquid assembly method [20–22]. In particular, Park et al. prepared a hierarchically structured composite consisting of reduced graphene oxide and WO_3 via hydrothermal and heating treatment. The composite showed a good reversible capacity of 487 mAh g^{-1} under 150 mA g^{-1} over 100 cycles [23]. Kim et al. fabricated the onion-like crystalline WS_2 nanoparticles anchored on graphene sheets [24]. This material exhibited a specific capacity of 356.5 mAh g^{-1} at 100 mA g^{-1} after 100 cycles. Pang and their coworkers grew WS_2 nanosheets on mesoporous carbon CMK-3 by hydrothermal approach; the resulting composite delivered a good specific capacity of

* Corresponding authors.
E-mail addresses: peter.comba@aci.uni-heidelberg.de (P. Comba), klingeler@kip.uni-heidelberg.de (R. Klingeler).

https://doi.org/10.1016/j.electacta.2023.142540
Received 23 January 2023; Received in revised form 21 April 2023; Accepted 5 May 2023
Available online 12 May 2023

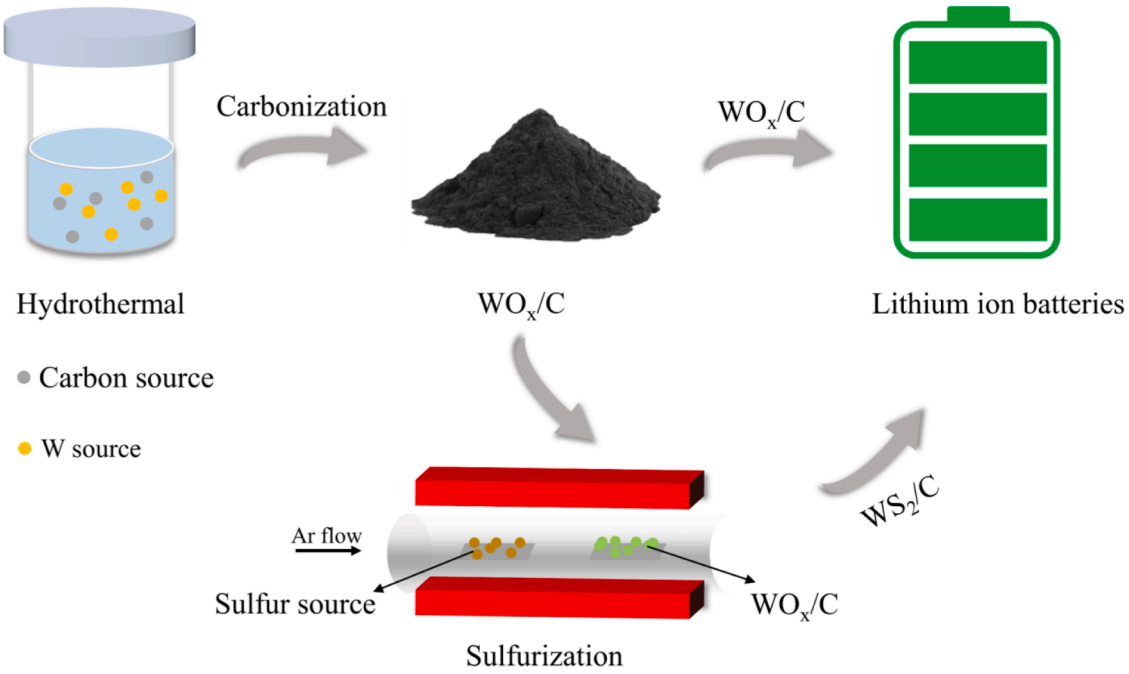

Scheme 1. Schematic illustration of the preparation of WO_x/C and WS_2/C composites.

720 mAh g^{-1} at 100 mA g^{-1} after 100 cycles [25].

Although the above composites exhibited better battery performance than the bare ones, complicated synthesis methods and high-cost carbonaceous materials still limit their practical application. Therefore, it is urgently needed to develop an easier and low-cost method to prepare composites of carbonaceous materials with metal oxides and sulfides. Polyvinyl pyrrolidone (PVP) and cetyltrimethylammonium bromide (CTAB) have been reported as low-cost carbon sources for various composites for many applications. For example, PVP was used as a carbon source to prepare MoS_2/C composites [26–28], carbon-coated SiO [29], SiO_2/C composite nanofibers [30], C@CoFe layered double hydroxides arrays [31], and V_2O_3@carbon nanofiber [32]. In the case of CTAB, it also worked as a carbon source for the preparation of carbon-coated TiO_2 [33], carbon-coated NaV_6O_{15} flower [34], nitrogen-doped Mo_2C@C composites [35], $Li_4Ti_5O_{12}$/C [36], and Ni-Mo_2C/graphene aerogel [37].

Here, we report a facile and scalable approach to fabricating carbon-coated metal oxides and sulfides by taking tungsten oxide and sulfide as an example. Two kinds of carbon sources, PVP and CTAB, were adopted to verify our approach. Important synthesis conditions, such as carbonization temperature, sulfurization temperature, and the amount of the carbon source, were adjusted. As a result, carbon-coated tungsten oxide and tungsten disulfide synthesized with two different carbon sources exhibit excellent battery performance. The reported approach provides an easy and versatile route that can be extended to the preparation of other metal oxides and disulfides.

2. Experimental section

2.1. Synthesis of WO_x/C composite

WO_x/C composites were synthesized by a hydrothermal process and subsequent carbonization. Firstly, 600 mg Na_2WO_4 was dissolved in 25 ml deionized water at room temperature, then 9 M HCl solution was added dropwise to adjust the pH of the mixture to 1.5. 200 mg or 500 mg carbon source (CTAB, PVP) was subsequently added to the solution. The mixture was transferred to a 50 ml stainless steel autoclave lined with PTFE and heated at 180℃ for 24h and then cooled to room temperature. The precipitate was collected after centrifugation, washed several times with water and ethanol, and dried in an oven at 80℃ for 24 h. Finally, the powder was sintered under a flow of Argon gas at 400 – 800℃ for two hours to obtain WO_x/C composites, which are denoted as c-WO_x/C and p-WO_x/C respectively (x is a value varying from 2 to 3) according to the carbon source (CTAB or PVP) used for the synthesis. Pristine WO_3 was fabricated using the same reaction conditions without adding a carbon source.

2.2. Synthesis of WS_2/C composite

In the giving step, WO_x/C composites were used as precursors and further sulfurized to WS_2/C. 100 mg WO_x/C composite was ground with 500 mg thiourea and then loaded into an alumina crucible which was put in the downstream of a tube furnace; other alumina boat containing 500 mg thiourea was put in the upstream. The tube furnace was then kept at 600 or 800℃ for 2 h under argon flow. Pristine WS_2 was fabricated using the same reaction conditions by sulfurization of pristine WO_3. Depending on the initial carbon source, either CTAB (c) or PVP (p), the obtained products are denoted as c/p-WS_2/C. Mixed-phase composites are labeled as c/p-WO_x/C-WS_2/C.

2.3. Material characterization

X-ray diffraction (XRD) patterns were obtained with a Bruker AXS D8 Advance Eco diffractometer using Cu K_α radiation and a step size of $\Delta(2\Theta) = 0.02^\circ$ at the angular scans. Scanning electron microscopy (SEM) was carried out with a ZEISS Leo 1530 scanning electron microscope. Transmission electron microscopy (TEM) and high-resolution TEM (HR-TEM) were performed on a Tecnai F30 transmission electron microscope (FEI Corporation, USA) at an acceleration voltage of 200 kV. The elemental mapping was performed on a scanning transmission electron microscope (STEM) unit with a high-angle annular dark-field (HAADF) detector (FEI, Tecnai F30) operating at an acceleration voltage of 200 kV. Thermogravimetric analysis (TGA) was conducted on a DTA-Q600 SDT TA at a heating rate of 10℃ min^{-1} from room temperature to 800℃ under flowing air. X-ray photoelectron spectroscopy (XPS) measurements were conducted using a MAX 200 (Leybold-Heraeus) spectrometer equipped with a hemispherical analyzer (EA 200; Leybold-Heraeus) and a Mg Kα X-ray source. The XP spectra were

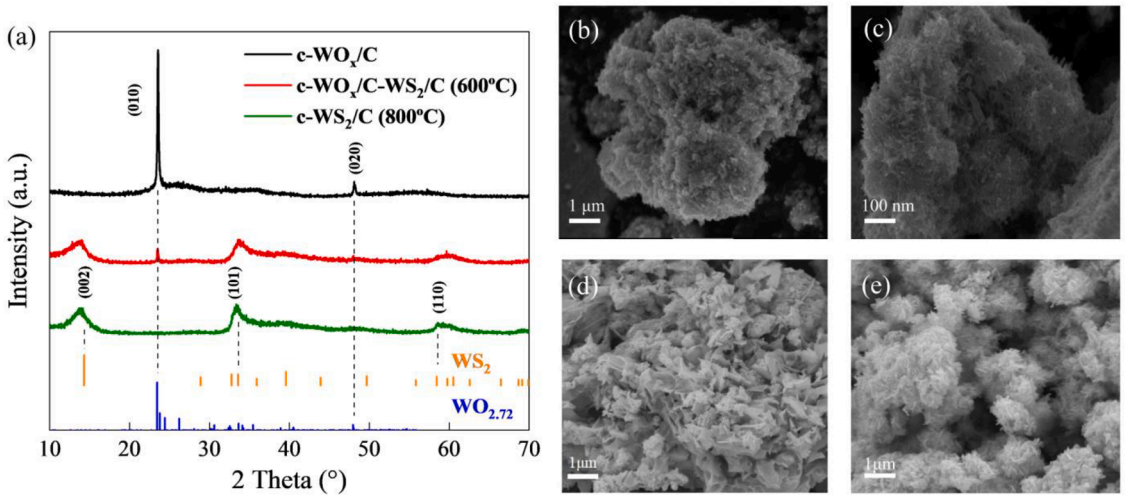

Fig. 1. (a) XRD patterns of c-WO_x/C, c-WO_x/C-WS_2/C (sulfurization at 600℃) and c-WS_2/C (sulfurization at 800℃). Vertical ticks show the reference patterns according to JCPDS No. 08-0237 and JCPDS No.71-2450. (b-e) SEM images of (b, c) c-WO_x/C, (d) c-WO_x/C-WS_2/C and (e) c-WS_2/C.

acquired in normal emission geometry with an energy resolution of ~0.9 eV. The binding energy (BE) scale of the spectra was referenced to the Au 4f $_{7/2}$ peak at 84.0 eV.

2.4. Battery assembly and electrochemical measurements

The electrochemical performance of the fabricated materials was evaluated using coin cells (CR2032). The working electrodes were prepared by mixing the active material with carbon black and polyvinylidene difluoride (PVDF, Solvay Plastics) at a mass ratio of 7:2:1 in 1-methyl-2-pyrrolidone (NMP, Sigma Aldrich) by magnetic stirring for at least 12 h [38]. The mixed slurry was then applied on circular Cu meshes (diameter 10 mm) with a mass loading of about 1.5-2 mg cm^{-2}. Afterward, the electrodes were dried at 80℃ under vacuum,

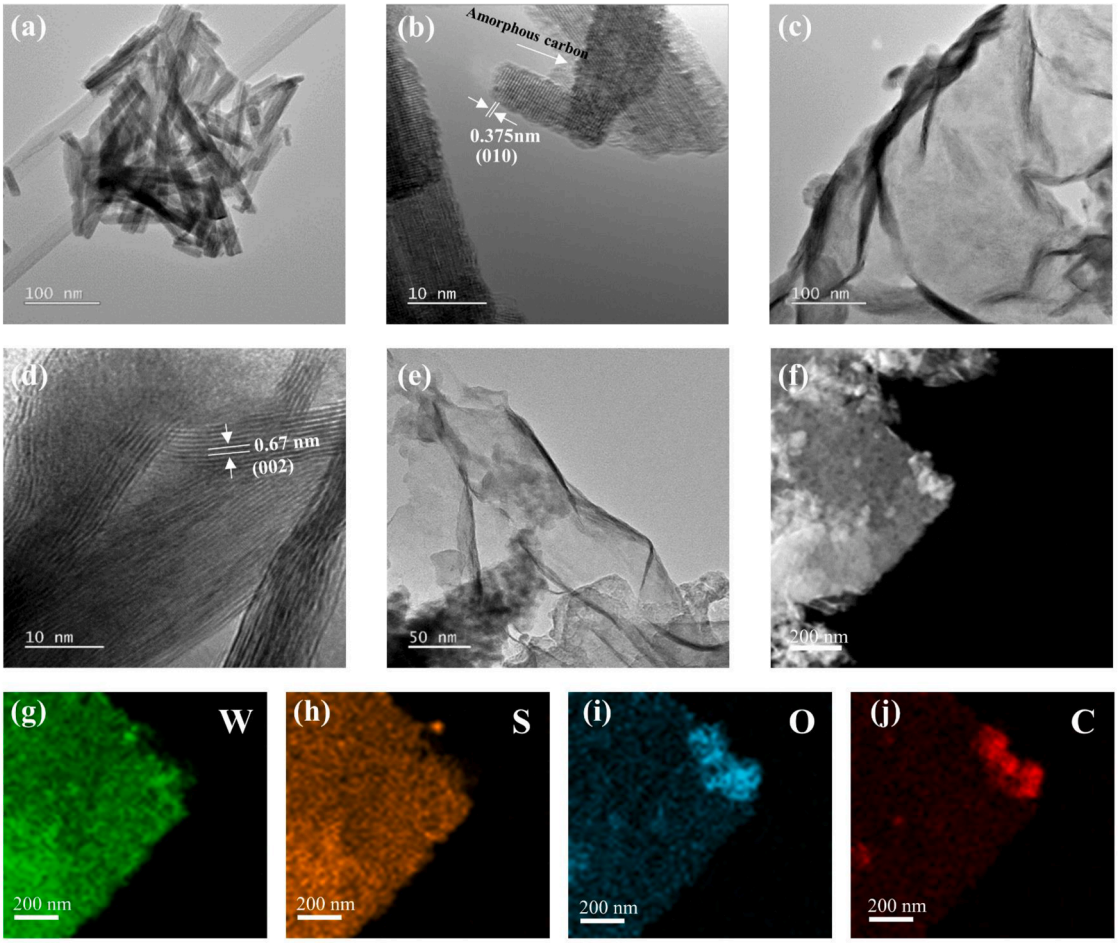

Fig. 2. TEM images and HR-TEM images of c-WO_x/C (a, b) and c-WS_2/C (c, d). TEM images (e, f) and elemental mapping images (g-j) of c-WO_x/C-WS_2/C.

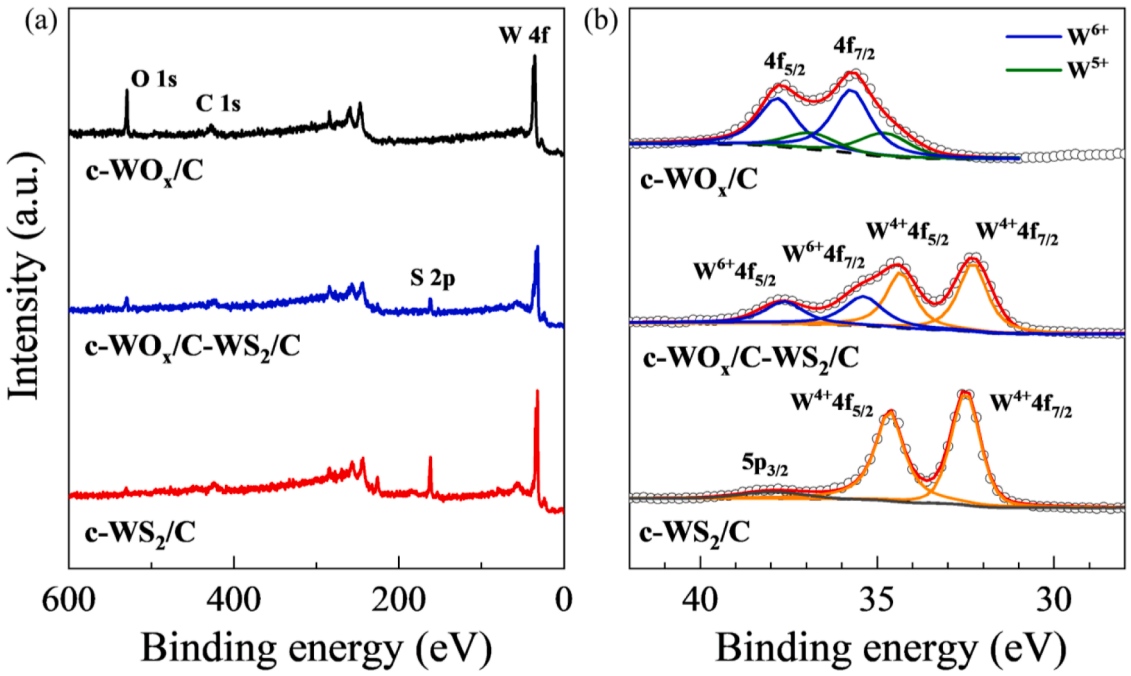

Fig. 3. Wide-scan XP spectra (a) and W 4f XP spectra (b) of c-WO_x/C, c-WO_x/C-WS_2/C, and c-WS_2/C. Characteristic peaks and doublet components are marked.

mechanically pressed at 10 MPa, and then dried again. The cells were assembled in a glove box under argon atmosphere ($O_2/H_2O < 5$ ppm) by using two layers of glass microfibre separator (WhatmanGF/D) soaked with 130 μl of a1 M solution of $LiPF_6$ in ethylene carbonate (EC)/dimethyl carbonate (DMC) (1:1 by volume) (LP30, Merck) and a lithium foil (Sigma Aldrich) pressed on a nickel plate as the counter electrode. The electrochemical properties were investigated by cyclic voltammetry and galvanostatic cycling with potential limitation (GCPL) in the voltage range from 0.01 to 3 V. The measurements were performed with a VMP3 potentiostat (BioLogic) at room temperature.

3. Results and discussion

The experimental synthesis procedure of WO_x/C and WS_2/C composites is illustrated in Scheme 1. The WO_x/C was obtained based on a hydrothermal process and a post-carbonization procedure. After a further sulfurization step, the WS_2/C was fabricated. It is noted that instead of high-cost carbonaceous materials like graphene, mesoporous carbon, and carbon nanotubes, the commonly used and inexpensive carbon source (CTAB and PVP) were introduced. Both carbon-coated tungsten oxides and disulfides could be easily obtained without the involvement of any sacrificial template and complex preparation steps. The effects of crucial synthesis parameters, such as the amount of carbon source, carbonization temperature, and sulfurization temperature, on the crystal structure, morphology, and battery performance of the above composite materials were investigated. We will first discuss the composites produced with the CTAB source, which was generally set to 500 mg.

3.1. c-WO_x/C, c-WO_x/C-WS_2/C, and c-WS_2/C

3.1.1. Morphology and structure of c-WO_x/C, c-WO_x/C-WS_2/C, and c-WS_2/C

XRD patterns of pristine c-WO_x/C, sulfurized at 600 and 800°C, respectively, are shown in Fig. 1a. The pattern of pristine c-WO_x/C exhibit distinct peaks at 23° and 48°, characteristic of $WO_{2.72}$ (JCPDS No. 71-2450) [39]. The influence of the amount of CTAB and the carbonization temperature on the obtained phase are presented in the Supplementary Information. A reduction of the amount of CTAB (200 mg) still results in the production of $WO_{2.72}$. Whereas without the addition of CTAB, the growth of pure WO_3 occurred (Fig. S1a). Besides, a high carbonization temperature (800°C) causes the formation of WO_2 (Fig. S1b). Thus, we conclude that CTAB also acts as a reducing agent during the carbonization in addition to serving as a carbon source, and this effect becomes stronger at higher temperatures.

Upon sulfurization, the characteristic $WO_{2.72}$-diffraction peaks are suppressed and new features at 13°, 32°and 60° appear, pointing to the presence of WS_2 (JCPDS No. 08-0237). When the sulfurization process is performed at 800°C, the resulting product is c-WS_2/C as indicated by the complete absence of the $WO_{2.72}$ diffraction peaks. By comparison, if the sulfurization temperature is 600°C, a mixture of two components (c-WO_x/c-WS_2/C) is formed (see Fig. 1a). It can thus be concluded that the degree of sulfurization is controlled by the sulfurization temperature [40]. Moreover, all peaks associated with WS_2 are rather broad, indicating poor crystallinity. The phase of WS_2 was maintained when a small amount of CTAB (200 mg) was added (Fig. S3a), which is similar to the case of $WO_{2.72}$. While phase purity is proven for c-WO_x and c-WS_2 within the limits of XRD resolution by the data in Fig. 1a, the presence of either of the materials is clearly demonstrated for c-WO_x/WS_2. Due to the width of the Bragg peaks which we mainly attribute to size effects and crystalline defects, as well as due to the anisotropic shape, the potential spatial alignment of the particles, and the presence of amorphous material, only a rough estimate of the crystalline WS_2 : WO_x ratio of 2:1 can be deduced from the data (68(10) % WS_2, 32(10) % WO_x).

The effect of sulfurization on the microstructure of the resulting composites is demonstrated by SEM images in Fig. 1b-e and TEM images in Fig. 2a-e. Pristine c-WO_x/C exhibits a nanocluster-like structure of agglomerated nanorods with 100 – 200 nm in length (Fig. 1b, c). For comparison, the mixed-phase c-WO_x/C-WS_2/C is composed of curled nanosheets as well as nanoparticles which are assumed to be c-WO_x/C and c-WS_2/C, respectively (Fig. 1d). After the complete sulfurization at 800°C, only curled nanosheets are observed in the resulting c-WS_2/C (Fig. 1e). Moreover, as shown in Fig. S2a, b and S3b, c, the morphology of c-WO_x/C and c-WS_2/C does not change noticeably at a small amount of CTAB added (200 mg). However, a low carbonization temperature (400°C) caused the production of irregular c-WO_x/C (Fig. S2c).

As the TEM ad HRTEM images shown in Fig. 2a, b, the c-WO_x/C nanorods are coated by amorphous carbon which agrees with its SEM

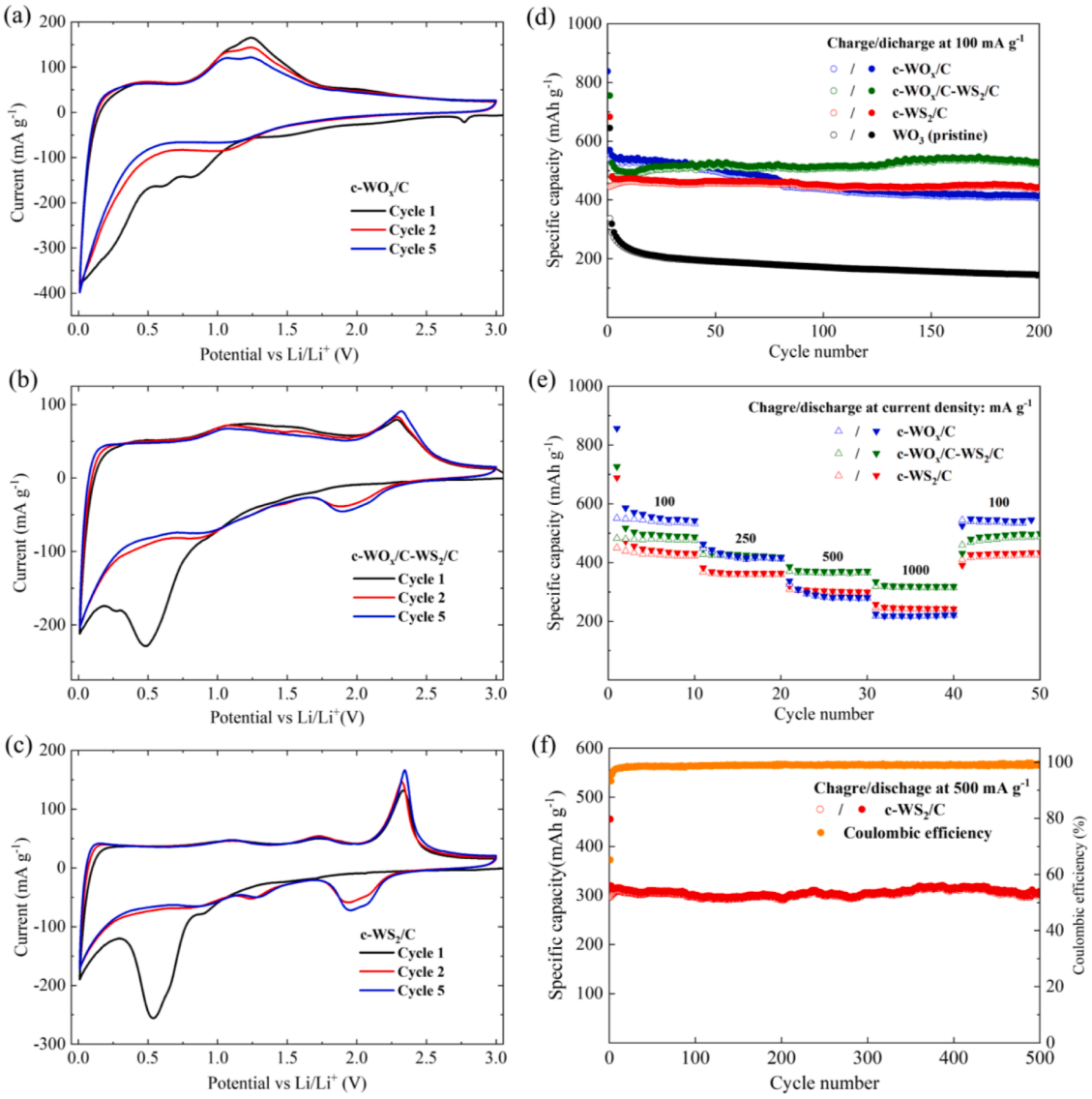

Fig. 4. CV curves for (a) c-WO_x/C, (b) c-WO_x/C-WS_2/C, and (c) c-WS_2/C electrodes for the first, second, and fifth cycles at a scan rate of 0.1 mV s^{-1} and in a potential range of 0.01–3 V vs. Li/Li^+. (d) Cycling performance at 100 mA g^{-1} and (e) rate performance of the above electrodes at the current densities ranging from 100 to 1000 mA g^{-1}. (f) Long-term cycling performance and Coulombic efficiency of c-WS_2/C at a high current density of 500 mA g^{-1}. In (d), the values for the pristine WO_3 are also shown for comparison.

images. The lattice fringes with a spacing of 0.375 nm can be indexed to the (010) planes, corresponding to the main peak of $WO_{2.72}$ in the XRD patterns. The TEM and HRTEM images of the resulting c-WS_2/C (Fig. 2c-d) exhibit curled nanosheets with an interlayer spacing of 0.675 nm, which can be attributed to the (002) plane of WS_2 [41,42]. The elemental mappings of c-WS_2/C by energy dispersive spectroscopy (EDS) shown in Fig. S4 confirm the uniform distribution of W, S, and C in this composite. In the mixed-phase, c-WO_x/C-WS_2/C, both WS_2 nanosheets and WO_x nanoparticles are observed, as seen in Fig. 2e, which is consistent with the corresponding SEM images. EDS elemental mapping, presented in Fig. 2g-j, further illustrates the homogenous distribution of W, O, S, and C within randomly selected areas in Fig. 2f, indicating the coexistence of c-WO_x/C and c-WS_2/C, which is in good agreement with the XRD data. Thermogravimetric analysis (TGA) curves (Fig. S5) demonstrate that the specific carbon contents in c-WO_x/C, c-WO_x/C-WS_2/C, and c-WS_2/C are about 2.0, 2.1, and 2.0 (±0.5) wt%, respectively.

Chemical states and compositions of c-WO_x, c-WO_x/C-WS_2/C, and c-WS_2/C were monitored by XPS. The wide-scan XP spectrum of c-WO_x/C shown in Fig. 3a confirms the presence of W, O, and C in this material. After the sulfurization, there is a clear signature of S, as seen in the wide-scan spectra of c-WO_x/C-WS_2/C and c-WS_2/C. Simultaneously, the signal of O gradually decreases in intensity due to the sulfurization treatment. All these observations agree well with the results of the EDS elemental mapping.

The W 4f XP spectrum of the c-WO_x/C composite shown in Fig. 3b exhibits a superposition of two W $4f_{7/2,5/2}$ doublets. The first doublet, with the component peaks at ~35.7 and ~37.8 eV, is attributed to W^{6+}. The second, comparably weak doublet, with the component peaks at ~34.9 eV and ~36.9 eV, is assigned to W^{5+}. One can thus conclude that c-WO_x/C is composed of W^{5+} and W^{6+}, in good agreement with the literature data [43]. In contrast, in the W 4f XP spectrum of c-WS_2/C, a single W $4f_{7/2,5/2}$ doublet, with the component peaks at 32.5 eV and 34.6 eV, is found, corresponding to the W^{4+} oxidation state [44]. This doublet is accompanied by a broad W $5p_{3/2}$ peak at 37.8 eV. Complementary information is provided by the S 2p XP spectrum of c-WS_2/C. The characteristic S $2p_{3/2,1/2}$ doublet, with the component peaks at 161.8 eV and 162.9 eV (Fig. S6), can be assigned to S−W bond,

confirming the presence of WS_2. Moreover, the very low intensity of the O 1s peak in the spectrum of c-WS_2/C (Fig. 3a) verifies a nearly complete conversion of WO_x/C to WS_2/C. Significantly, the W 4f XP spectrum of the mixed-phase, c-WO_x/C-WS_2/C, confirms the presence of both W^{4+} and W^{6+}. Specifically, this spectrum exhibits two W $4f_{7/2,\ 5/2}$ doublets, with the component peaks at 32.2 eV and 34.4 eV for the first one and the component peaks at 5.5 eV and 37.7 eV for the second one. A coexistence of WO_x/C and WS_2/C in c-WO_x/C-WS_2/C is thus confirmed.

3.1.2. *Lithium ion storage performance of c-WO_x/C, c-WO_x/C-WS_2/C, and c-WS_2/C*

To investigate the electrochemical behaviors of c-WO_x/C, c-WO_x/C-WS_2/C, and c-WS_2/C electrodes, cyclic voltammetry (CV) at a scan rate of 0.1 mV s^{-1} and galvanostatic cycling with potential limitation (GCPL) were performed. The current density was set to either 100 or 500 mA g^{-1} and the potential window was set from 0.01 V to 3 V.

Fig. 4a shows the first, second, and fifth CV cycles of the c-WO_x/C electrode. The first cathodic scan displays five reduction peaks. Peaks at 2.8 and 0.6 V correspond to irreversible reactions and the formation of solid electrolyte interface (SEI) which disappear in the subsequent cycles. Other two reduction peaks at 1.5 and 0.8 V can be assigned to the lithium intercalation into $WO_{2.72}$ (Eq. (1)). The peak located at 0.3 V is attributed to the conversion reaction of $Li_xWO_{2.72}$ (Eq. (2)). During the first anodic process, an oxidation peak appears at 1.25 V which is associated with the delithiation process of Li_2O (Eq. (3)) [41,45].

In the second discharge cycle, only one reduction peak at 1.1 V, corresponding to the lithium insertion into $WO_{2.72}$ (Eq. (1)), is visible. This peak is representative of a similar electrochemical reaction as the reduction peaks in the first cathodic scan but its position is slightly different, which can be attributed to structural changes caused by irreversible conversion reactions during the initial cycling [45]. The second and fifth CV cycles are mostly overlapping, implying high reversibility of Li^+ storage in the c-WO_x/C electrode after the second cycle.

The relevant electrochemical reactions for c-WO_x/C can be expressed below [45]:

$$WO_{2.72} + xLi^+ + xe^- \leftrightarrow Li_x\ WO_{2.72} \quad (1)$$

$$Li_x\ WO_{2.72} + (5.44 - x)Li^+ + (5.44 - x)e^- \rightarrow W + 2.72Li_2O \quad (2)$$

$$Li_2O + W \rightarrow xWO_{2.72} + (2 - x)W + zLi_2O + (2 - 2z)Li^+ + (2 - 2z)e^- \quad (3)$$

The c-WS_2/C electrode exhibits a completely different electrochemical behavior as shown by the respective CV curves in Fig. 4c. In the first cathodic scan, three reduction peaks are observed. The ones at 1.6 and 0.9 V can be attributed to the lithiation of WS_2 to form Li_xWS_2 (Eq. (4)). The third reduction peak, centered at 0.6 V, corresponds to the conversion reaction from Li_xWS_2 to metallic W (Eq. (5)) as well as to the generation of SEI [46,47]. Also, in the first anodic scan, three oxidation peaks are recorded. Two of them, at 1.1 and 1.7 V, are fingerprints of the delithiation of Li_xWS_2 to form WS_2 (Eq. (4)). The pronounced oxidation peak at 2.3 V is associated with the oxidation of Li_2S to S (Eq. (6)) [47]. In the subsequent cathodic scan, three new reduction peaks appear which are ascribed to the lithiation of WS_2 (features at 0.9 and 1.3 V) (Eq. (4)) and the formation of Li_2S (1.9 V). At the same time, the reduction peak at 0.6 V disappears, indicating the irreversibility of the conversion reaction.

The electrochemical processes for c-WS_2/C can be described as follows:

$$WS_2 + xLi^+ + xe^- \leftrightarrow Li_x\ WS_2 \quad (4)$$

$$Li_x\ WS_2 + (4 - x)Li^+ + (4 - x)e^- \rightarrow 2Li_2\ S + W \quad (5)$$

$$2Li_2\ S \leftrightarrow 4Li^+ + 4e^- + 2S \quad (6)$$

The oxidation peaks in the second anodic scan are overlapping with the ones in the first cycle. Besides, the CV profiles remain fairly consistent and steady in the fifth cycle, suggesting good reversibility and stability of lithium ion transport.

For the mixed-phase, c-WO_x/C-WS_2/C, the CV profile in Fig. 4b displays the fingerprints of both constituting materials. Specifically, three reduction peaks in the first cathodic scan at 1.0, 0.5, and 0.3 V emphasize the intercalation of lithium ions into $WO_{2.72}$ and WS_2, the formation of an SEI, and the conversion reactions of WS_2 and $WO_{2.72}$, respectively. Oxidation peaks in the first anodic scan correspond to the delithiation of Li_xWO_x and Li_xWS_2 (1.1 V) and the delithiation of WS_2 (2.3 V). Similarly, in the further cycles, features related to WO_x/C as well as to WS_2/C are observed thereby showing that both materials in this mixed phase contribute to the electrochemical behavior. Again, the good matching of the redox peaks in the second and fifth cycles indicates high reversibility of Li^+ storage in the c-WO_x/C-WS_2/C electrode.

Fig. S7 shows the galvanostatic charge-discharge profiles for the 1^{st}, 2^{nd}, 10^{th}, 100^{th} and 200^{th} cycles of c-WO_x/C, c-WO_x/C-WS_2/C, and c-WS_2/C electrodes at a current density of 100 mA g^{-1}. The observed potential plateaus are in good agreement with the CV results. The corresponding cycling performances and Coulombic efficiency are shown in Fig. 4d and Fig. S8 where the data of the pristine WO_3 electrode are also presented for comparison. The pristine electrode shows an initial specific discharge/charge capacity of 645/338 mAh g^{-1} which decreases gradually to 198/197 mAh g^{-1} after 200 cycles. The reason behind this decrease is typically assigned to the volume expansion effects and poor electric conductivity [39]. In contrast, the carbon-coated c-WO_x/C electrode not only delivers a higher initial specific discharge/charge capacity of 840/560 mAh g^{-1} but also exhibits noticeably better capacity retention (74%) which still amounts to 420 mAh g^{-1} after 200 cycles. For comparison, if a relatively small amount of CTAB (200 mg) is used, the initial specific discharge/charge capacity (860/630 mAh g^{-1}) is slightly higher than for the "standard" amount of CTAB (500 mg) but the capacity retention value (48%) is noticeably lower (Fig. S9). This can be explained by the lower carbon content resulting from the smaller amount of CTAB, which is not enough to completely cover WO_x. By contrast, the sufficiently high carbon content (500 mg) provides the full carbon coating on the WO_x surface, which not only promotes the electron and lithium ion diffusion kinetics but also alleviates the pulverization and volume expansion of WO_x [48].

The c-WO_x/C electrode exhibits a faster capacity fading in the first 20 cycles (Fig. S10) and the specific capacity is gradually maintained in the following cycles if the carbonization temperature is set to 400℃. Interestingly, a capacity retention of 88% is observed after nearly 100 cycles for the c-WO_x/C electrode synthesized at the high carbonization temperature (800℃), but the low initial specific discharge/charge capacity of 630/420 mAh g^{-1} hinders its application. The above results imply that the parameters of the preparation procedure, such as carbonization temperature and the amounts of carbon source, play crucial roles in the battery performance of the synthesized c-WO_x/C.

After sulfurization at 600℃, c-WO_x/C was partially converted to c-WS_2/C, and the mixed-phase, c-WO_x/C-WS_2/C, was obtained. In comparison with the c-WO_x/C electrode, the c-WO_x/C-WS_2/C electrode shows enhanced cycling stability as well as slightly lower initial specific discharge/charge capacities of 760/530 mAh g^{-1}. After 200 cycles, the specific discharge capacity of this electrode is remarkably maintained at 525 mAh g^{-1} (99% capacity retention) and no obvious capacity fading is observed during the cycling.

The full sulfurization of c-WO_x/C to c-WS_2/C at 800℃ provides an electrode with an initial discharge/charge capacity of 680/483 mAh g^{-1}. Besides, this electrode shows remarkable cycling stability (95% capacity retention) and a high discharge capacity of 460 mAh g^{-1}, which is close to the theoretical capacity of WS_2 (462 mAh g^{-1}), after 200 cycles.

The pristine WS_2 and c-WS_2/C electrodes prepared with a small amount of CTAB (200 mg) were also tested to verify the importance of carbon coating. The respective pristine WS_2 electrode displays a fast discharge capacity fading from 836 to 248 mAh g^{-1} after 60 cycles

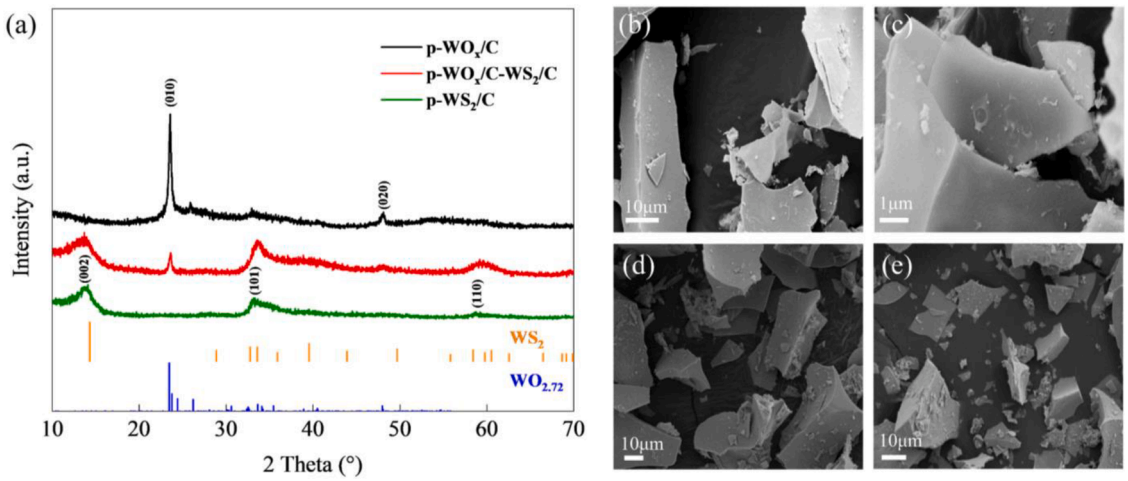

Fig. 5. (a) XRD patterns of p-WO_x/C, p-WO_x/C-WS_2/C (sulfurization at 600°C), and p-WS_2/C (sulfurization at 800°C). Vertical ticks show the reference patterns according to JCPDS No. 08-0237 and JCPDS No.71-2450. (b-e) SEM images of (b, c) p-WO_x/C, (d) p-WO_x/C-WS_2/C, and (e) p-WS_2.

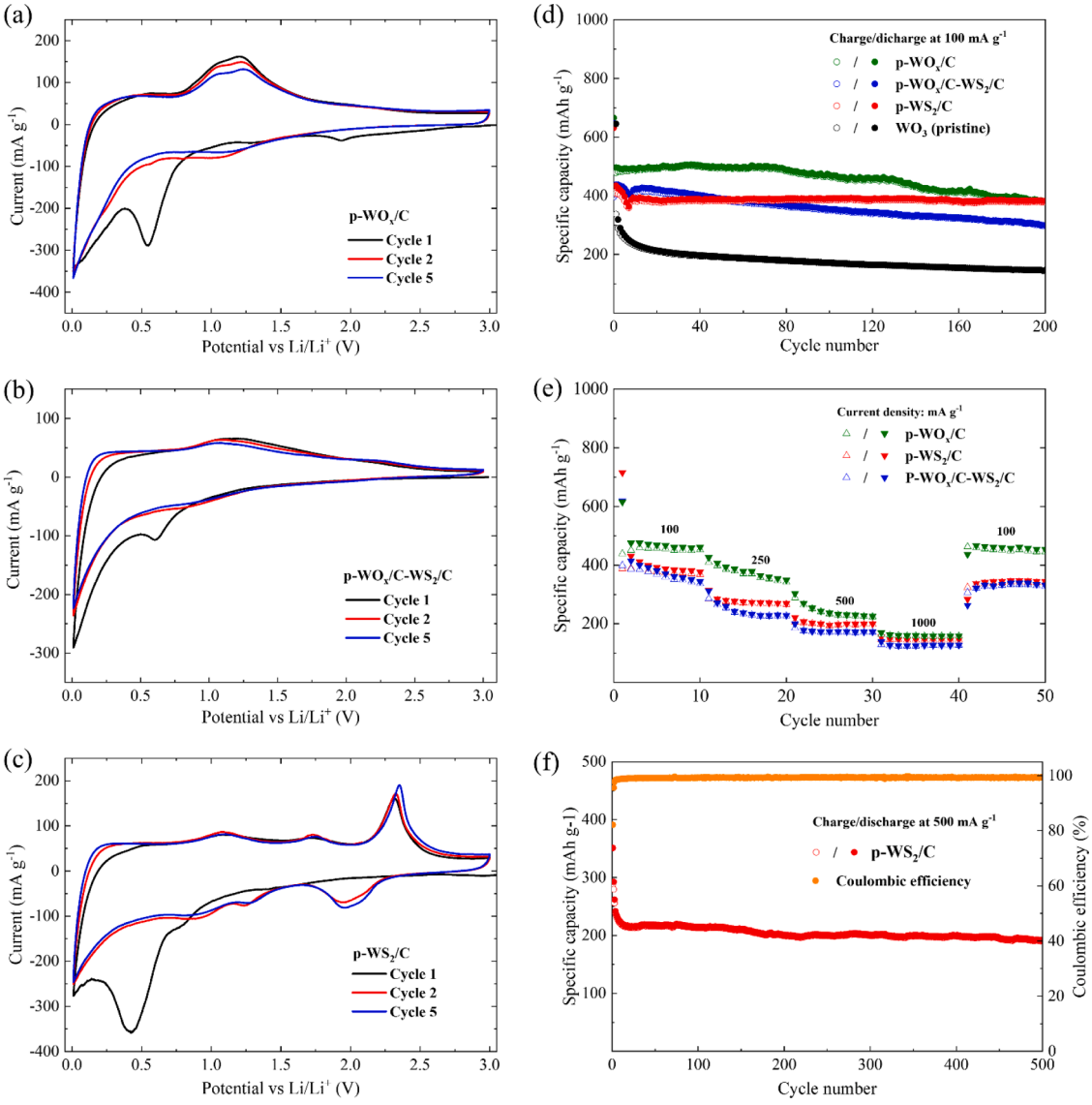

Fig. 6. CV curves for (a) p-WO_x/C, (b) p-WO_x/C-WS_2/C, and (c) p-WS_2/C electrodes for the first, second, and fifth cycles at a scan rate of 0.1 mV s^{-1} in a potential range of 0.01–3 V versus Li/Li^+. (d) Cycling performance at 100 mA $g^{-1}$and (e) rate performance of the above electrodes at current densities ranging from 100 to 1000 mA g^{-1}. (f) Long-term cycling performance and Coulombic efficiency of p-WS_2/C at a high current density of 500 mA g^{-1}.

(Fig. S11). The c-WS_2/C electrode has a high initial capacity but shows a significant capacity drop from 763 to 428 mAh g^{-1} after 100 cycles (Fig. S11). Hence, optimization of the amounts of CTAB for the c-WS_2/C is of importance.

In brief, the electrodes of c-WO_x/C and c-WS_2/C as well as mixed-phase c-WO_x/C-WS_2/C all exhibit better cycling performance and higher specific capacities than the pristine WO_3 and WS_2 electrodes implying the usefulness of the facile composite preparation method described here.

Additionally, as shown in Fig. 4e, the rate capabilities of the c-WO_x/C, c-WO_x/C-WS_2/C, and c-WS_2/C electrodes were tested under different current densities ranging from 100 to 250, 500, and 1000 mA g^{-1}. The c-WS_2/C electrode delivers average specific discharge/charge capacities of 440, 360, 300, and 250 mAh g^{-1}, respectively. As the current density is returned to 100 mAg^{-1}, the specific discharge/charge capacity quickly recovers to 435 mAh g^{-1}. Similar superior rate performances are also observed for the c-WO_x/C-WS_2/C electrode which shows slightly higher average specific discharge/charge capacities of 500, 420, 380, and 320 mAh g^{-1}, respectively, at the same current densities. Consequently, both c-WS_2/C and c-WO_x/C-WS_2/C electrodes display high reversibility and excellent rate capability. By comparison, the c-WO_x/C electrode exhibits slightly inferior rate capability, delivering specific capacities of 550, 420, 280, and 220 mAh g^{-1}, respectively.

Motivated by the excellent stability and rate performance of the c-WS_2/C electrode, its long-term stability was evaluated at a high current density of 500 mA g^{-1}. Remarkably, as shown in Fig. 4f, even over 500 cycles, a high capacity retention of 97% is obtained and the electrode delivers a capacity of 307 mAh g^{-1}.

3.2. p-WO_x/C, p-WO_x/C-WS_2/C, and p-WS_2/C

3.2.1. Morphology and structure of p-WO_x/C, p-WO_x/C-WS_2/C, and p-WS_2/C

In order to confirm the general applicability of the presented preparation method, PVP was used as an alternative carbon source to prepare carbon-coated tungsten-based oxide and disulfide. Analogously to the case of CTAB, p-WO_x/C was firstly synthesized via a hydrothermal and carbonization process, and then sulfurized at 600 and 800°C to be converted into p-WO_x/C-WS_2/C and p-WS_2/C, respectively.

Fig. 5a shows the XRD patterns of p-WO_x/C, p-WO_x/C-WS_2/C, and p-WS_2/C. In the case of p-WO_x/C, two main peaks at 23° and 48° are observed, corresponding to the (010), and (020) planes of $WO_{2.72}$, respectively. It is noteworthy that, similar to CTAB, PVP worked as a carbon source as well as a reducing agent. After p-WO_x/C was further sulfurized at 600°C, three new peaks located at 13°, 32°, and 60° appeared which are attributed to the (002), (102), and (110) planes of WS_2. When the sulfurization temperature was elevated to 800°C, the peaks characteristic of $WO_{2.72}$ disappeared, while the peaks characteristic of WS_2 remained. It can then be concluded that the use of CTAB and PVP results in similar products, which confirms the general character of the preparation method. Similar to what has been found for the CTAB-based materials, the mixed PVP-assisted compound features a WS_2 : WO_x ratio of about 2:1 (66(10) % WS_2, 34(10) % WO_x). Some differences were however recorded. In contrast to the regular structure of the c-WO_x/C particles, the morphology of p-WO_x/C turned out to be quite irregular exhibiting microparticles ranging from 2 to 50 μm as well as some microplates (Figs. 5b, c). It is notable that this irregular morphology is maintained after sulfurization to p-WO_x/C-WS_2/C and p-WS_2/C (Figs. 5d, e), which differs noticeably from the behavior of the CTAB-based composites for which the morphology changed from nanorods to nanosheets after the sulfurization. The TEM and HRTEM images (Fig. S12) confirm the SEM data. Moreover, TEM-EDS mappings (Figs. S13 and S14), show a uniform distribution of the elements, including W, O, S, and C as well as W, S, and C in p-WO_x/C-WS_2/C and p-WS_2/C, respectively. As shown in Fig. S15, the carbon contents in p-WO_x/C, p-WO_x/C-WS_2/C, and p-WS_2/C amount to 11.6, 13.9, and 12.1 (±0.5) wt% respectively. Accordingly, we conclude that PVP provides more carbon coating than CTAB under identical preparation conditions.

3.2.2. Lithium ion storage performance of p-WO_x/C, p-WO_x/C-WS_2, and p-WS_2/C

The electrochemical behaviors of p-WO_x/C, c-WO_x/C-WS_2/C, and p-WS_2/C electrodes, as studied by CV (Figs. 6a, b, and c) and GCPL measurements (Figs. S16a, b, and c) in analog to section 3.1.2, is very similar to the materials obtained by the CTAB-assisted syntheses. The cycling performance and Coulombic efficiency of pristine WO_3, p-WO_x/C, p-WO_x/C-WS_2/C, and p-WS_2/C electrodes were studied and the results are shown in Fig. 6d and Fig. S17. Compared with the pristine WO_3 electrode, the p-WO_x/C electrode delivers a lower initial discharge/charge specific capacity of 660/480 mAh g^{-1}, but exhibits more stable cycling performance (80% capacity retention after 200 cycles) at 100 mA g^{-1}. The mixed-phase p-WO_x/C-WS_2/C electrode, however, does not show an obvious improvement in battery performance compared with the p-WO_x/C electrode. It delivers an initial discharge/charge specific capacity of 630/440 mAh $g^{-1}$and a capacity retention of 67% after 200 cycles at 100 mA g^{-1}. In the case of the CTAB-assisted mixed-phase, c-WO_x/C-WS_2/C, the big improvement in the cycling stability can be explained by the synergetic effect of c-WO_x/C and c-WS_2/C. However, the micro-scale structure of p-WO_x/C-WS_2/C might mitigate the impact of this effect and lead to worse capacity retention. As p-WO_x/C completely converted to p-WS_2/C at 800°C, the p-WS_2/C electrode delivers a comparatively low initial discharge/charge specific capacity of 654/420 mAh g^{-1} but shows excellent stability, viz. a capacity retention of 90% after 200 cycles at 100 mA g^{-1}.

To evaluate the rate capabilities, the p-WO_x/C, p-WO_x/C-WS_2/C, and p-WS_2/C electrodes were cycled at various current densities ranging from 100 mA g^{-1} to 1000 mA g^{-1} with 10 cycles for each (Fig. 6e). The p-WO_x/C and p-WO_x/C-WS_2/C electrodes show a pronounced capacity decrease along with increasing current densities. In contrast, the p-WS_2/C electrode exhibits an excellent rate performance, delivering high reversible capacities of 390, 280, 200, and 150 mAh g^{-1} and fast recovering to 360 mAh g^{-1} as the current density returns to 100 mA g^{-1}. In addition, the long-life cycling performance of p-WS_2/C electrode was tested at a current density of 500 mA g^{-1} to further verify its cycling stability. As displayed in Fig. 6f, a capacity retention of 80% is attained after 500 cycles, suggesting a superior cycling performance.

In the context of the above results, it is worth noting that CTAB works as a growth controller, setting the preferential orientation of WO_x and causing the formation of nanorods [49]. And the subsequent sulfurization process leads to the growth of the WS_2 curled nanosheets. These unique nanostructures provide both short lithium-ion diffusion paths and high surface areas [21]. Meanwhile, the carbon coating of around 2wt% (Table S1) can not only accommodate the volume expansion of WO_x and WS_2 during the cycling process but also improve the electrical conductivity of composites [24]. As a consequence, the unique structures and carbon coating result in outstanding cycling stability and the excellent rate capability of CTAB-assisted composites. Besides, in the mixed phase c-WO_x/C-WS_2/C, the content of WS_2 is estimated two times higher than that of WO_x (Table S1), leading to more electrochemical contribution from WS_2 and thus the comparatively lower capacity for the mixed phase than that for c-WO_x/C. By comparison, the PVP-assisted composites show a higher carbon content of 11wt%-14wt% (Table S1) and the high-content carbon coating hinders the lithium-ion diffusion, causing low capacity [48]. Although a similar ratio of WO_x and WS_2 was realized in the mixed phase p-WO_x/C-WS_2/C to the CTAB-assisted counterpart, the capacity retention is comparatively unstable. This might be because the unfavorable morphology of microparticles and microplates makes the volume expansion difficult to be alleviated even with the help of carbon coating and this effect works strongly in tungsten oxides instead of tungsten disulfide due to the moderate volume expansion of metal sulfides [15]. But both CTAB and PVP-assisted composites exhibit significantly enhanced lithium storage performance

Table 1
Electrochemical performance of various tungsten oxides and sulfides composites in LIBs.

Active material	Current (mA g^{-1})	Cycle number	Capacity (mAh g^{-1})	Ref.
WO_{3-x}/C nanosheets	200	100	662	[17]
m-WO_x /C	250	100	443	[18]
Cauliflower-like WO_3@C composites	50	50	650	[50]
WS_2/carbon nanotube-reduced graphene oxide	200	100	556	[21]
Polygonal WS_2@graphene multilayer films	100	100	430	[51]
WS_2@Super P nanocomposites	100	200	389	[52]
WS_2 nanoflowers@carbon nanotube vines	1000	140	455	[53]
WS_2 nanosheets@cabon composites	100	100	322	[54]
Carbon coated WO_x	100	200	420	This work
Carbon coated WO_x-WS_2	100	200	525	
Carbon coated WS_2	100/500	200/500	460/307	

compared to the bare tungsten oxide and disulfide. To highlight the improvement, Table 1 compares the previously reported electrochemical performances of various tungsten oxides and sulfides composites when used as electrode materials in LIBs. The table implies competitive specific capacities and superior cycling stability of the carbon-coated tungsten oxides and sulfides produced in our work exhibit.

4. Conclusion

In summary, we developed a facile and useful method for the synthesis of carbon-coated tungsten oxides and disulfides. Two kinds of carbon sources (PVP, CTAB) were adopted to obtain WO_x/C, WS_2/C, and mixed-phase, WO_x/C-WS_2/C. The respective composite electrodes exhibit excellent lithium-ion battery performance. Specifically, the c-WO_x/C electrode delivers a high initial discharge/charge capacity of 840/560 mAh g^{-1} at 100 mA g^{-1} and a 74% capacity retention after 200 cycles. Significantly, the c-WO_x/C-WS_2/C and c-WS_2/C electrodes show outstanding cycling stability with capacity retention of 99% and 95% respectively, after 200 cycles at 100 mA g^{-1}. Besides, the c-WS_2/C electrode also features a capacity retention of 97% after 500 cycles at a high current density of 500 mA g^{-1}. In addition, the p-WO_x/C, p-WS_2/C, and WO_x/C-WS_2/C electrodes exhibit high potential for high-performance lithium-ion storage. In particular, p-WS_2/C shows a capacity retention of 80% after 500 cycles at 500 mA g^{-1}. Hence, the proposed fabrication method provides a simple and low-cost way to prepare carbon-coated tungsten oxides and disulfides, useful in the context of high-performance lithium storage.

CRediT authorship contribution statement

Peng Guo: Conceptualization, Methodology, Synthesis, Investigation, Data analysis, Writing – original draft, Review & editing. **Lennart Singer:** Data analysis, Investigation (SEM). **Zhiyong Zhao:** Investigation, Data analysis (XPS). **Wojciech Kukułka, Ewa Mijowska:** Investigation (TEM, EDX-SEM). **Finn Sebastian:** Investigation (CV, GCPL). **Michael Zharnikov:** Investigation, Data analysis (XPS), Review & editing. **Peter Comba, Rüdiger Klingeler:** Supervision, Conceptualization, Review & editing.

Declaration of Competing Interest

The authors declare that they have no known competing financial interests or personal relationships that could have appeared to influence the work reported in this paper.

Data availability

Data will be made available on request.

Acknowledgments

We are grateful for access to the instrument and technical support for SEM studies provided by J. Zaumseil's group at Heidelberg University. This work was supported by the Deutsche Forschungsgemeinschaft DFG via KL 1824/12-1, within the framework of the Excellence Strategy of the Federal and State Governments of Germany, and through the China Scholarship Council (CSC). The authors thank I. Glass for experimental support.

Supplementary materials

Supplementary material associated with this article can be found, in the online version, at doi:10.1016/j.electacta.2023.142540.

References

[1] S. Koohi-Fayegh, M.A. Rosen, A review of energy storage types, applications and recent developments, J. Energy Storage 27 (2020).
[2] W. Li, X. Guo, P. Geng, M. Du, Q. Jing, X. Chen, G. Zhang, H. Li, Q. Xu, P. Braunstein, H. Pang, Rational Design and General Synthesis of Multimetallic Metal-Organic Framework Nano-Octahedra for Enhanced Li-S Battery, Adv. Mater. 33 (2021), e2105163.
[3] P. Geng, L. Wang, M. Du, Y. Bai, W. Li, Y. Liu, S. Chen, P. Braunstein, Q. Xu, H. Pang, MIL-96-Al for Li-S Batteries: Shape or Size? Adv. Mater. 34 (2022), e2107836.
[4] J. Gu, Y. Peng, T. Zhou, J. Ma, H. Pang, Y. Yamauchi, Porphyrin-based framework materials for energy conversion, Nano Research Energy 1 (2022), e9120009.
[5] N. Nitta, F. Wu, J.T. Lee, G. Yushin, Li-ion battery materials: present and future, Mater. Today 18 (2015) 252–264.
[6] P. Roy, S.K. Srivastava, Nanostructured anode materials for lithium ion batteries, J. Mater. Chem. A 3 (2015) 2454–2484.
[7] A. Manthiram, An Outlook on Lithium Ion Battery Technology, ACS Cent. Sci. 3 (2017) 1063–1069.
[8] Z. Li, A. Ottmann, T. Zhang, Q. Sun, H.-P. Meyer, Y. Vaynzof, J. Xiang, R. Klingeler, Preparation of hierarchical C@MoS_2@C sandwiched hollow spheres for lithium ion batteries, J. Mater. Chem. A 5 (2017) 3987–3994.
[9] X. Yu, C. Pei, W. Chen, L. Feng, 2 dimensional WS_2 tailored nitrogen-doped carbon nanofiber as a highly pseudocapacitive anode material for lithium-ion battery, Electrochim. Acta 272 (2018) 119–126.
[10] L. Zhang, H.B. Wu, X.W.D. Lou, Iron-Oxide-Based Advanced Anode Materials for Lithium-Ion Batteries, Adv. Energy Mater. 4 (2014).
[11] B. Xiao, G. Wu, T. Wang, Z. Wei, Y. Sui, B. Shen, J. Qi, F. Wei, J. Zheng, High-entropy oxides as advanced anode materials for long-life lithium-ion Batteries, Nano Energy 95 (2022).
[12] Y. Zhang, P. Wang, Y. Yin, N. Liu, N. Song, L. Fan, N. Zhang, K. Sun, Carbon coated amorphous bimetallic sulfide hollow nanocubes towards advanced sodium ion battery anode, Carbon 150 (2019) 378–387.
[13] M. Zheng, H. Tang, Q. Hu, S. Zheng, L. Li, J. Xu, H. Pang, Tungsten-Based Materials for Lithium-Ion Batteries, Adv. Funct. Mater. 28 (2018).
[14] W. Dang, W. Wang, Y. Yang, Y. Wang, J. Huang, X. Fang, L. Wu, Z. Rong, X. Chen, X. Li, L. Huang, X. Tang, One-step hydrothermal synthesis of 2D WO_3 nanoplates@graphene nanocomposite with superior anode performance for lithium ion battery, Electrochim. Acta 313 (2019) 99–108.
[15] Y. Zhang, P. Wang, Y. Yin, X. Zhang, L. Fan, N. Zhang, K. Sun, Heterostructured SnS-ZnS@C hollow nanoboxes embedded in graphene for high performance lithium and sodium ion batteries, Chem. Eng. J. 356 (2019) 1042–1051.
[16] Z. Li, F. Yuan, M. Han, J. Yu, Atomic-Scale Laminated Structure of O-Doped WS_2 and Carbon Layers with Highly Enhanced Ion Transfer for Fast-Charging Lithium-Ion Batteries, Small 18 (2022), e2202495.
[17] K. Bao, W. Mao, G. Liu, L. Ye, H. Xie, S. Ji, D. Wang, C. Chen, Y. Li, Preparation and electrochemical characterization of ultrathin WO_{3-x} /C nanosheets as anode materials in lithium ion batteries, Nano Res. 10 (2016) 1903–1911.
[18] C. Jo, W.-G. Lim, A.H. Dao, S. Kim, S. Kim, S. Yoon, J. Lee, Tracking the confinement effect of highly dispersive carbon in a tungsten oxide/carbon nanocomposite: conversion anode materials in lithium ion batteries, J. Mater. Chem. A 5 (2017) 24782–24789.
[19] K. Shiva, H.S.S. Ramakrishna Matte, H.B. Rajendra, A.J. Bhattacharyya, C.N. R. Rao, Employing synergistic interactions between few-layer WS_2 and reduced

graphene oxide to improve lithium storage, cyclability and rate capability of Li-ion batteries, Nano Energy 2 (2013) 787–793.
[20] R. Chen, T. Zhao, W. Wu, F. Wu, L. Li, J. Qian, R. Xu, H. Wu, H.M. Albishri, A.S. Al-Bogami, D.A. El-Hady, J. Lu, K. Amine, Free-standing hierarchically sandwich-type tungsten disulfide nanotubes/graphene anode for lithium-ion batteries, Nano Lett. 14 (2014) 5899–5904.
[21] Y. Wang, D. Kong, W. Shi, B. Liu, G.J. Sim, Q. Ge, H.Y. Yang, Ice Templated Free-Standing Hierarchically WS_2/CNT-rGO Aerogel for High-Performance Rechargeable Lithium and Sodium Ion Batteries, Adv. Energy Mater. 6 (2016).
[22] T. Li, R. Guo, Y. Luo, F. Li, L. Meng, X. Sun, Z. Yang, H. Luo, Y. Wan, Improved lithium and sodium ion storage properties of WS_2 anode with three-layer shell structure, Electrochim. Acta 331 (2020).
[23] S.K. Park, H.J. Lee, M.H. Lee, H.S. Park, Hierarchically structured reduced graphene oxide/WO_3 frameworks for an application into lithium ion battery anodes, Chem. Eng. J. 281 (2015) 724–729.
[24] I. Kim, S.-W. Park, D.-W. Kim, Onion-like crystalline WS_2 nanoparticles anchored on graphene sheets as high-performance anode materials for lithium-ion batteries, Chem. Eng. J. 375 (2019).
[25] Q. Pang, Y. Gao, Y. Zhao, Y. Ju, H. Qiu, Y. Wei, B. Liu, B. Zou, F. Du, G. Chen, Improved Lithium-Ion and Sodium-Ion Storage Properties from Few-Layered WS_2 Nanosheets Embedded in a Mesoporous CMK-3 Matrix, Chem. 23 (2017) 7074–7080.
[26] Y. Li, L. Zan, J. Chen, Improving the Reaction Kinetics by Annealing MoS_2/PVP Nanoflowers for Sodium-Ion Storage, Molecules 28 (2023).
[27] M. Liu, N. Li, S. Wang, Y. Li, C. Liang, K. Yu, 3D nanoflower-like MoS_2 grown on wheat straw cellulose carbon for lithium-ion battery anode material, J. Alloys Compd. 933 (2023).
[28] J. Shao, Q. Qu, Z. Wan, T. Gao, Z. Zuo, H. Zheng, From Dispersed Microspheres to Interconnected Nanospheres: Carbon-Sandwiched Monolayered MoS_2 as High-Performance Anode of Li-Ion Batteries, ACS Appl. Mater. Interfaces 7 (2015) 22927–22934.
[29] Z. Huang, G. Dang, W. Jiang, Y. Sun, M. Yu, Q. Zhang, J. Xie, A Low-Cost and Scalable Carbon Coated SiO-Based Anode Material for Lithium-Ion Batteries, ChemistryOpen 10 (2021) 380–386.
[30] A. Belgibayeva, I. Taniguchi, Synthesis and characterization of SiO_2/C composite nanofibers as free-standing anode materials for Li-ion batteries, Electrochim. Acta 328 (2019).
[31] S.M. Xu, X. Liang, X.Y. Wu, S.L. Zhao, J. Chen, K.X. Wang, J.S. Chen, Multistaged discharge constructing heterostructure with enhanced solid-solution behavior for long-life lithium-oxygen batteries, Nat. Commun. 10 (2019) 5810.
[32] C. Busacca, O. Di Blasi, N. Briguglio, M. Ferraro, V. Antonucci, A. Di Blasi, Electrochemical performance investigation of electrospun urchin-like V_2O_3-CNF composite nanostructure for vanadium redox flow battery, Electrochim. Acta 230 (2017) 174–180.
[33] Y. Li, C. Chen, M. Wang, W. Li, Y. Wang, L. Jiao, H. Yuan, Excellent sodium storage performance of carbon-coated TiO_2: Assisted with electrostatic interaction of surfactants, J. Power Sources 361 (2017) 326–333.
[34] Y. Dong, J. Xu, M. Chen, Y. Guo, G. Zhou, N. Li, S. Zhou, C.-P. Wong, Self-assembled NaV_6O_{15} flower-like microstructures for high-capacity and long-life sodium-ion battery cathode, Nano Energy 68 (2020).
[35] Y. Liu, B. Huang, X. Hu, Z. Xie, Surfactant-assisted hydrothermal synthesis of nitrogen doped Mo_2C@C composites as highly efficient electrocatalysts for hydrogen evolution reaction, Int. J. Hydrogen Energy 44 (2019) 3702–3710.
[36] K. Liu, J. Cui, J. Yin, J. Man, Y. Cui, Z. Wen, J. Sun, Ultra-long life core-shell structure $Li_4Ti_5O_{12}$/C nanocomposite anode materials for lithium ion batteries, J. Alloys Compd. 765 (2018) 229–235.
[37] P. Kumar, M. Arumugam, G. Maia, S. Praserthdam, P. Praserthdam, Double role of CTAB as a surfactant and carbon source in Ni-Mo_2C/GA composite: As a highly active electrocatalyst for hydrogen evolution reaction, Electrochim. Acta (2023) 441.
[38] E. Thauer, G.S. Zakharova, L.F. Deeg, Q. Zhu, R. Klingeler, Hierarchically structured V_2O_3/C microspheres: Synthesis, characterization, and their electrochemical properties, Electrochim. Acta 390 (2021).
[39] W. Zhang, L. Yue, F. Zhang, Q. Zhang, X. Gui, R. Guan, G. Hou, N. Xu, One-step in situ synthesis of ultrathin tungsten oxide@carbon nanowire webs as an anode material for high performance, J. Mater. Chem. A 3 (2015) 6102–6109.
[40] B. Zhang, C. Luo, Y. Deng, Z. Huang, G. Zhou, W. Lv, Y.B. He, Y. Wan, F. Kang, Q. H. Yang, Optimized Catalytic WS_2–WO_3 Heterostructure Design for Accelerated Polysulfide Conversion in Lithium–Sulfur Batteries, Adv. Energy Mater. 10 (2020).
[41] Y. Sun, W. Wang, J. Qin, D. Zhao, B. Mao, Y. Xiao, M. Cao, Oxygen vacancy-rich mesoporous $W_{18}O_{49}$ nanobelts with ultrahigh initial Coulombic efficiency toward high-performance lithium storage, Electrochim. Acta 187 (2016) 329–339.
[42] L. Yin, D. Pham-Cong, I. Jeon, J.-P. Kim, J. Cho, S.-Y. Jeong, H.Woo Lee, C.-R. Cho, Electrochemical performance of vertically grown WS_2 layers on $TiNb_2O_7$ nanostructures for lithium-ion battery anodes, Chem. Eng. J. 382 (2020).
[43] L. Sinha, P.M. Shirage, Surface Oxygen Vacancy Formulated Energy Storage Application: Pseudocapacitor-Battery Trait of $W_{18}O_{49}$ Nanorods, J. Electrochem. Soc. 166 (2019) A3496–A3503.
[44] J. Li, H. Yan, W. Wei, X. Li, L. Meng, Enhanced Lithium Storage Performance of Liquid-Phase Exfoliated Graphene Supported WS_2 Heterojunctions, ChemElectroChem 5 (2018) 3222–3228.
[45] Z. Chen, K. Ye, M. Li, S. Zhao, J. Luo, B. Wu, Lithiation mechanism of $W_{18}O_{49}$ anode material for lithium-ion batteries: Experiment and first-principles calculations, J. Electroanal. Chem. 880 (2021).
[46] H. Liu, D. Su, G. Wang, S.Z. Qiao, An ordered mesoporous WS_2 anode material with superior electrochemical performance for lithium ion batteries, J. Mater. Chem. 22 (2012).
[47] H.T. Huu, H.T.T. Le, V.P. Nguyen, T.T. Huong Nguyen, T.X. Dieu Nguyen, V. T. Nguyen, S.-J. Kim, V. Vo, Facile one-step synthesis of g–C_3N_4–supported WS_2 with enhanced lithium storage properties, Electrochim. Acta 341 (2020).
[48] W. Sun, Z. Hu, C. Wang, Z. Tao, S.L. Chou, Y.M. Kang, H.K. Liu, Effects of Carbon Content on the Electrochemical Performances of MoS_2-C Nanocomposites for Li-Ion Batteries, ACS Appl. Mater. Interfaces 8 (2016) 22168–22174.
[49] X.L. Xu, Y. Chen, S.Y. Ma, S.H. Yan, Y.Z. Mao, T. Wang, H.Q. Bian, CTAB-assisted synthesis of unique 3D ZnO and the acetone sensing performances, Mater. Lett. 151 (2015) 5–8.
[50] S. Yoon, S.-G. Woo, K.-N. Jung, H. Song, Conductive surface modification of cauliflower-like WO_3 and its electrochemical properties for lithium-ion batteries, J. Alloys Compd. 613 (2014) 187–192.
[51] Y. Dong, S. Chen, J. Liu, J. Lei, F. Liu, W. Yang, J. Wang, Polygonal WS_2-decorated-graphene multilayer films with microcavities prepared from a cheap precursor as anode materials for lithium-ion batteries, Mater. Lett. 254 (2019) 73–76.
[52] J. Huang, X. Wang, J. Li, L. Cao, Z. Xu, H. Wei, WS_2-Super P nanocomposites anode material with enhanced cycling stability for lithium ion batteries, J. Alloys Compd. 673 (2016) 60–66.
[53] X. Li, J. Zhang, Z. Liu, C. Fu, C. Niu, WS_2 nanoflowers on carbon nanotube vines with enhanced electrochemical performances for lithium and sodium-ion batteries, J. Alloys Compd. 766 (2018) 656–662.
[54] J. Li, X. Shi, J. Fang, J. Li, Z. Zhang, Facile Synthesis of WS_2 Nanosheets-Carbon Composites Anodes for Sodium and Lithium Ion Batteries, ChemNanoMat 2 (2016) 997–1002.